JPE 17-3-18

https://doi.org/10.6113/JPE.2017.17.3.756
ISSN(Print): 1598-2092 / ISSN(Online): 2093-4718

An Improved Control Method for Power Conversion System under a Weak Grid by the Adoption of Virtual Resistors

Ning Gao†, Shun Sang*, Rui Li*, and Xu Cai*

†,*Wind Power Research Center, School of Electronic Information and Electrical Engineering, Shanghai Jiao Tong University, Shanghai, China

Abstract

The control of the power conversion system (PCS) in a battery energy storage system has a challenge due to the existence of grid impedance. This paper studies an impedance model of an LCL-based PCS in the *d-q* domain. The feature of a PCS connected to a weak grid is unveiled by use of an impedance model and a generalized Nyquist criterion. It is shown that the interaction between grid impedance and the PCS destabilizes the cascaded system in certain cases. Therefore, this paper proposes a novel control method that adopts virtual resistors to overcome this issue. The improvement in the control loop leads the PCS to a more stable condition than the conventional method. Impedance measurement is implemented to verify the correctness of the theoretical analysis. Experimental results obtained from a down-scaled prototype indicate that the proposed control method can improve the performance of the PCS under a weak grid.

Key words: Battery energy storage system, Impedance model, Power conversion system, Virtual resistors

I. INTRODUCTION

In recent years, more attention has been paid to the integration of sustainable energy sources (SES), such as wind power and PV, with utilities in order to decrease global energy consumption[1][2]. Unfortunately, sustainable energy sources deteriorate the power quality of the grid due to their intermittent and fluctuating natures. To overcome this issue, it is essential to install an energy storage system in the vicinity of SESs for the purpose of smoothing output power to a dispatchable level. This is especially mandatory for power grids with massive SES penetration [3], [4].

There are several options for different energy storage systems (ESS), like flywheels, super capacitors, compressed air, battery ESS (BESS) and so on [5]. Among these options, BESSs appear as a popular choice to compensate the fluctuating power generated by SESs because of their large capacity, long cycle life, high energy density and fast response [6], [7]. The power conversion system is regarded as the core component of a BESS [8]. In this paper, the PCS can be assumed to be a specific bidirectional DC-AC inverter that is particularly utilized in ESS applications, and interfaces battery units with the grid based on power electronics technology to convert alternating current to direct current [9]-[11]. Decoupled current-control based on the synchronous reference frame (also named the *d-q* frame) is widely adopted in PCSs for independently tracking the active and reactive power references [12]. Either from the view of accuracy or dynamic response, this control method has been proved to have good performance for grid connecting inverter control.

However, sometimes a BESS is located near SESs in remote areas due to abundant resources. A typical example is a BESS applied in an offshore wind farm [13], where the local electric power system is connected with the main grid through long transmission lines and a series of distribution transformers. Depending on the grid configuration, the high grid impedance that is mainly produced by the parasitic inductance of lines and transformers rapidly reduces the short circuit carrying capacity. In these cases, a local electric power system, also named "weak grid", can no longer be assumed to be an ideal voltage source. The impedance in a non-ideal grid condition can interact with a

Manuscript received Sep. 20, 2016; accepted Jan. 17, 2017
Recommended for publication by Associate Editor Jae-Do Park.
†Corresponding Author: gaoning@sjtu.edu.cn
Tel: +86-21-34207001, Fax: +86-21-34207470, Shanghai Jiao Tong Univ.
*Wind Power Research Center, School of Electronic Information and Electrical Engineering, Shanghai Jiao Tong University, China

PCS by unpredictably changing the characteristics of the grid filter and the response of control loop [14]. This can lead to harmonic resonance and grid voltage distortion [15], [16], as well as instability and black-out events under certain circumstances [17]. Therefore, it is worthwhile to study and improve the stability of PCSs in the presence of large grid impedance variations.

To solve the aforementioned problems, the authors of [18] applied the impedance concept in a grid-tied inverter, which is assumed as a more advantageous approach for analyzing the stability of an inverter under a weak grid because it avoids the necessity of remodeling every inverter when the grid impedance changes. The authors of [19] modeled a three-phase converter by a positive-sequence and a negative-sequence impedance in the phase domain. The authors of [20] developed a small-signal impedance model of three-phase converters with an L filter in the d-q domain based on the harmonic linearization thesis. The authors of [21] studied the influence of PLLs as a supplement to [20]. These two kinds of models, named the sequence impedance model and the d-q impedance model, are further validated in [22]-[24]. They are also used to analyze the sub-synchronous resonance phenomenon and voltage stability in a WT-MMC-HVDC cascaded system.

In practice, unlike [20] and [21], many grid-tied inverters adopt passive filters based on an LCL or other high order structures since they can provide better performance in terms of switching harmonics attenuation. However, these filters are inherently resonant and might destabilize the overall system. Some active damping methods are discussed in [25], [26] to overcome this shortcoming. However, their performance under a weak grid has not been studied. The authors of [27] applied an impedance-based stability analysis in a single-phase inverter and then proposed an impedance-phased compensation strategy as a solution to enhance the robust stability. However, it is more complex to extend this strategy to a three-phase inverter.

This paper is organized as follows. Section I briefly depicts the principle of PCS. Then section II deduces the impedance model of a three-phase LCL-based PCS as an effective diagnostic tool when comparing different control methods. In addition, the influence of grid impedance is analyzed by the use of a compatible stability criterion. Then a novel control method involving virtual resistors is proposed in section III to improve the performance of PCS under a weak grid. This is followed by a similar procedure for the stability analysis employed in the prior section. Experimental results obtained with a down-scaled laboratory prototype are demonstrated in section IV to confirm the feasibility of the proposed control method. Finally, section V gives a conclusion to this paper.

II. IMPEDANCE MODEL DERIVATION OF PCS

Fig.1 shows a graphical representation of a BESS circuit and its control block diagram. In Fig.1, the battery is the main static

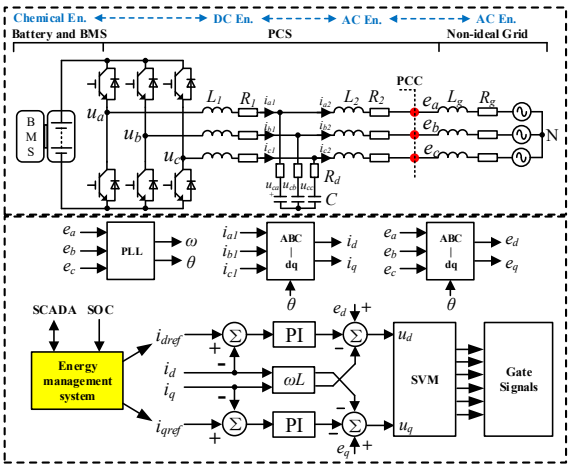

Fig. 1. Block diagram of a BESS.

energy storage component based on its internal chemical reactions, together with a battery management system (BMS) as an indispensable accessory to achieve precise estimation of the state of charge (SOC). In the analysis of the PCS, the battery is equivalent to a stiff DC voltage source as its output voltage variation only depends on the SOC. On the other hand, the PCS consists of a two-level three-phase voltage source converter (VSC) including six insulated gate bipolar transistors anti-paralleled with free-wheeling diodes, and a passive filter based on LCL construction.

The traditional current feedback control implemented in the grid voltage oriented *d-q* frame is usually applied in a PCS to realize power transfers commanded from an upstream SCADA. By doing a transformation from *a-b-c* frame to *d-q* frame, the AC system is reduced to a two order DC system, making it possible to trace i_d and i_q with no static error simply by adopting two PI regulators. What is more, only in a DC system, it is possible to derive a small-signal impedance model of PCS around its static working point via the traditional linearization theory[18]. Define the transformation matrix T_{dq} as:

$$T_{dq}=\frac{2}{3}\begin{bmatrix}\sin(\theta) & \sin(\theta-120^\circ) & \sin(\theta+120^\circ)\\ \cos(\theta) & \cos(\theta-120^\circ) & \cos(\theta+120^\circ)\end{bmatrix} \quad (1)$$

According to the fundamental of the impedance-based stability analysis theory presented in [18], the PCS could be regarded as an ideal current source *I(s)* parallel with an output impedance Z_{out} in the form of a Norton equivalent circuit. Meanwhile, a weak grid is equal to an ideal voltage source connected in series with an inductive impedance Z_g. Fig. 2 describes the overall cascaded system in the s-domain. The left part of Fig. 2 represents a PCS and right part represents a non-ideal grid. Notice that the PCS is defined as a load. All of the variables are expressed within the *d-q* frame in the form of either vectors or matrices.

As shown in Fig. 2, $E_g(s)$ is a 2x1 vector representing a small voltage perturbation near a static working point, while $I_g(s)$ is the small signal response generated by $E_g(s)$. The current

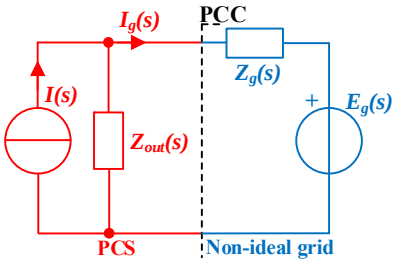

Fig. 2. Impedance representation of a PCS and non-ideal grid.

source $I(s)$ is naturally stable because a current controlled PCS is able to work stably when Z_g is equal to zero. Thus, it is unnecessary to pay a lot of attention to derive a complicated expression of $I(s)$. Z_g and Z_{out} are both 2x2 matrices, which represent the equivalent impedance of the grid and the PCS, respectively. A common expression of Z_g is given as:

$$Z_g = \begin{bmatrix} Z_{gdd} & Z_{gdq} \\ Z_{gqd} & Z_{gqq} \end{bmatrix} = \begin{bmatrix} sL_g + R_g & -\omega L_g \\ \omega L_g & sL_g + R_g \end{bmatrix} \tag{2}$$

Where R_g represents the resistive part of the grid impedance and L_g represents the inductive part. Based on the circuit model shown in Fig. 2, the output current disturbance in the point of common coupling (PCC), denoted as $\tilde{I}_g(s)$, can be expressed as:

$$\tilde{I}_g(s) = \frac{\left[I(s) - \tilde{E}_g(s)/Z_{out}(s)\right]}{\left[I + Z_g(s)/Z_{out}(s)\right]} \tag{3}$$

As discussed in [18], whether a PCS can operate stably is only dependent on the reciprocal of formula (3) due to the native stability of $I(s)$ and E_g/Z_{out}. That is to say, due to the obvious resemblance of the transfer function to a classic unity negative feedback control loop, the overall system is stable if the ratio of Z_g to Z_{out} satisfies the generalized Nyquist criterion (GNC). Since Z_g has already been given in Eq. (2), the derivation of the analytical expression of Z_{out} is the only challenge that needs to be discussed in detail.

First of all, E_g has no effect on $I(s)$. Hence, the current source $I(s)$ can be identified as an open circuit in the derivation procedure. Then similar as using the Voltage-ampere law to measure the impedance of passive networks, Z_g can be set to zero first. Based on this assumption, Z_{out} of the PCS can be derived by finding the relationship between E_g and I_g. Z_{out} satisfies the equation:

$$\begin{bmatrix} \tilde{e}_d^s \\ \tilde{e}_q^s \end{bmatrix} = -Z_{out} \begin{bmatrix} \tilde{i}_{d2} \\ \tilde{i}_{q2} \end{bmatrix} = -\begin{bmatrix} Z_{dd} & Z_{dq} \\ Z_{qd} & Z_{qq} \end{bmatrix} \begin{bmatrix} \tilde{i}_{d2} \\ \tilde{i}_{q2} \end{bmatrix} \tag{4}$$

Z_{dd} and Z_{qq} represent the impedance in the d and q channels, respectively. Meanwhile, Z_{dq} and Z_{qd} represent the coupling effect between the d and q channels. In order to derive Z_{out}, according to Eq.(4), the block diagram of the PCS is shown in Fig. 3.

It can be deduced from this diagram that the characteristic of the impedance is influenced both by the main circuit and the

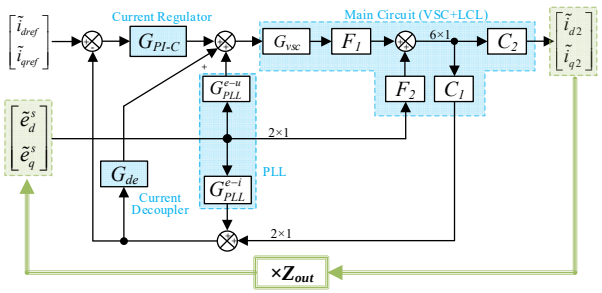

Fig. 3. Small-signal model of the PCS.

control parameters. Fig. 3 mainly includes three independent segments: the current regulator and decoupler, the phase locked loop (PLL) and the main circuit. To obtain the complete expression of Z_{out}, the transfer function of these three segments are needed to be deduced first. For the small-signal analysis, the disturbance of i_{dref} and i_{qref} is assumed to be zero.

(a) Modelling of the current regulator and decoupler.

The control principle generally used in the PCS usually applies two independent proportional integral (PI) regulators in the d-axis and q-axis respectively within the current loop. In Fig. 3, $G_{pi\text{-}c}$ represents these two regulators, and its matrix form is:

$$G_{PI-C} = \begin{bmatrix} k_{p-c} + k_{i-c}/s & 0 \\ 0 & k_{p-c} + k_{i-c}/s \end{bmatrix} \tag{5}$$

G_{DE} decouples the d-axis and q-axis components of the output current. This term should also be taken into account in the analysis. G_{DE} is given by Eq.(6).

$$G_{DE} = \begin{bmatrix} 0 & -\omega_0(L_1 + L_2) \\ \omega_0(L_1 + L_2) & 0 \end{bmatrix} \tag{6}$$

(b) Modelling of the main circuit.

The power circuit in the PCS mainly consists of two parts: the first is a VSC, represented by G_{vsc}, the second is an LCL filter, represented by F_1 and F_2. C_1 and C_2 are the auxiliary matrices, which make the mathematical derivation and description easier. The VSC often works in the PWM mode. The duty cycle is modulated sinusoidally by a high frequency carrier. In practice, the switching frequency f_s of the semiconductor devices in the VSC is usually chosen to be several kilo Hertz, which is much higher than 50Hz or 60Hz line frequency. In a relatively lower frequency range, the VSC is usually regarded as a static gain element K_{pwm} to represent the modulation procedure. This gain element K_{pwm} is connected in series with a unit delay representing the sampling and computational time cost in a digital control system. The unit delay is approximately equal to a one-order low-pass filter by using a Talor's expansion. Thus, the expression of G_{vsc} is given as:

$$G_{vsc} = K_{pwm} G_{delay} \approx \frac{K_{pwm}}{sT_s + 1} \tag{7}$$

The LCL filter is a high order passive filter widely adopted

in grid-tied inverters. It is more complex than a single L filter, with an improved effects on the suppression of switching frequency harmonics. As shown in Fig. 1 and Fig. 3, an LCL filter in a three-phase PCS has six state variables in the *d-q* frame. Thus, the state space *x* is defined as:

$$x = \begin{bmatrix} i_{d1} & i_{q1} & i_{d2} & i_{q2} & u_{cd} & u_{cq} \end{bmatrix}^T \tag{8}$$

Both C_1 and C_2 are projection transformation matrices to select a subspace from the total state space *x*. Wherein:

$$C_1 = \begin{bmatrix} 1 & 0 & 0 & 0 & 0 & 0 \\ 0 & 1 & 0 & 0 & 0 & 0 \end{bmatrix} \tag{9}$$

$$C_2 = \begin{bmatrix} 0 & 0 & 1 & 0 & 0 & 0 \\ 0 & 0 & 0 & 1 & 0 & 0 \end{bmatrix} \tag{10}$$

The input vector *u* is defined as:

$$u = \begin{bmatrix} u_d & u_q & e_d & e_q \end{bmatrix}^T \tag{11}$$

Then the LCL filter can be described by the state space formula as:

$$\frac{dx}{dt} = Ax + Bu \tag{12}$$

In formula (12), the expressions of matrix *A* and matrix *B* can be found in the appendix. By solving the state transition equation, matrix *F* can be identified as:

$$F = \left(sI - A\right)^{-1} B \tag{13}$$

F can be restructured into two 6-by-2 sub-matrices by doing a partition:

$$F_{(6\times4)} = \begin{bmatrix} F_{1(6\times2)} & F_{2(6\times2)} \end{bmatrix} \tag{14}$$

In these two 6x2 sub matrices, F_1 is related to the grid voltage, and F_2 is related to the output voltage of the PCS. F_1 and F_2 describe the final model of the LCL filter.

(c) Modelling of the PLL.

Generally, a software PLL implemented in a digital processor can be assumed as a common observer to estimate the actual grid angle θ^s to provide a synchronous reference θ^c to internal the *d-q* frame within the controller. A similar technique is widely adopted in flux observation of the motor driver. In this section, the superscript *c* represents the observed variables in the PLL, and the superscript *s* represents true variables in the circuit to avoid confusion.

In the PCS control, all of the voltage and current signals are sampled and rotated to controller's the *d-q* frame by θ^c while the modulation voltage is inversely rotated by the same reference. Therefore, the error between θ^s and θ^c, which is caused by the grid voltage perturbations, should be taken into account because it affects both the performance of the current loop and the modulation accuracy.

As Indicated in Fig. 3, these affects are represented by the transfer function matrix G_{pll}^{e-i} in the propagation path from the grid perturbation to the current perturbation, and by G_{pll}^{e-u} from the grid voltage perturbation to the output voltage perturbation. In order to derive these two transfer functions, a three-phase PLL strategy is illustrated in Fig. 4. It can be seen that θ^c is obtained from the positive feedback of e_q^c, which is regulated with a subsequent PI regulator denoted as $G_{pi\text{-}pll}$. The line frequency feedforward helps the PLL converge faster. The expression of $G_{pi\text{-}pll}$ is given as:

$$G_{PI-PLL} = k_{p-pll} + k_{i-pll} / s \tag{15}$$

In the steady state, θ^c is always equal to θ^s. Thus, the relationship in Eq.(16) always exists:

$$\begin{bmatrix} E_d^c \\ E_q^c \end{bmatrix} = \begin{bmatrix} \sin 90^\circ & -\cos 90^\circ \\ \cos 90^\circ & \sin 90^\circ \end{bmatrix} \begin{bmatrix} E_d^s \\ E_q^s \end{bmatrix} = \begin{bmatrix} E_d^s \\ E_q^s \end{bmatrix} \tag{16}$$

Adding the disturbance to Eq.(16) yields:

$$\begin{bmatrix} E_d^c + \tilde{e}_d^c \\ E_q^c + \tilde{e}_q^c \end{bmatrix} = \begin{bmatrix} \sin\left(90^\circ + \tilde{\theta}^c\right) & -\cos\left(90^\circ + \tilde{\theta}^c\right) \\ \cos\left(90^\circ + \tilde{\theta}^c\right) & \sin\left(90^\circ + \tilde{\theta}^c\right) \end{bmatrix} \times \begin{bmatrix} E_d^s + \tilde{e}_d^s \\ E_q^s + \tilde{e}_q^s \end{bmatrix} \tag{17}$$

By an approximation on the basis of trigonometric functions and elimination of the steady state variables, Eq.(17) can be simplified to:

$$\begin{bmatrix} \tilde{e}_d^c \\ \tilde{e}_q^c \end{bmatrix} \approx \begin{bmatrix} 1 & \tilde{\theta}^c \\ -\tilde{\theta}^c & 1 \end{bmatrix} \begin{bmatrix} \tilde{e}_d^s \\ \tilde{e}_q^s \end{bmatrix} \tag{18}$$

The relationship expressed by Eq. (19) exists in the forward path of the PLL shown in Fig. 4.

$$\tilde{\theta}^c = \tilde{e}_q^c \cdot G_{PI-PLL} \cdot \frac{1}{s} \tag{19}$$

Then combining Eq. (15) to Eq. (19), the observed voltage is equal to:

$$\begin{bmatrix} \tilde{e}_d^c \\ \tilde{e}_q^c \end{bmatrix} = \begin{bmatrix} 1 & 0 \\ 0 & 1 - E_d^s \cdot \dfrac{G_{PI-PLL}}{s + E_d^s \cdot G_{PI-PLL}} \end{bmatrix} \begin{bmatrix} \tilde{e}_d^s \\ \tilde{e}_q^s \end{bmatrix} \tag{20}$$

Likewise, the expressions of G_{pll}^{e-i} and G_{pll}^{e-u} can be derived by a similar procedure. The expressions are given in Eq. (21) and Eq.(22).

$$G_{pll}^{e-i} = \begin{bmatrix} 0 & I_{q1}^s \cdot \dfrac{G_{PI-PLL}}{s + E_d^s \cdot G_{PI-PLL}} \\ 0 & -I_{d1}^s \cdot \dfrac{G_{PI-PLL}}{s + E_d^s \cdot G_{PI-PLL}} \end{bmatrix} \tag{21}$$

$$G_{pll}^{e-u} = \begin{bmatrix} 0 & -U_q^c \cdot \dfrac{G_{PI-PLL}}{s + E_d^s \cdot G_{PI-PLL}} \\ 0 & U_d^c \cdot \dfrac{G_{PI-PLL}}{s + E_d^s \cdot G_{PI-PLL}} \end{bmatrix} \tag{22}$$

Let $\tilde{e}_q^s = E_d^s \times \tilde{\theta}^s$. Then Eq.(20) can be rewritten as:

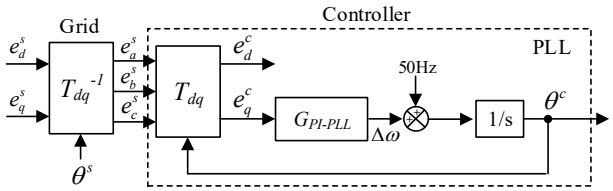

Fig. 4. Block diagram of the PLL.

TABLE I
DOWNSCALED PROTOTYPE PARAMETERS.

Parameter	Value
Rated power	500W
Grid voltage (line to line/RMS)	60V
Rated phase current (RMS)	5A
Grid frequency	50Hz
Switching frequency	10kHz
Dead band	3μs
Inverter-side inductor	1.65mH
Grid-side inductor	0.45mH
Filter capacitor	56μF
Battery capacity	100V/20Ah/ $LiFePO_4$

$$\frac{\tilde{\theta}^c}{\tilde{\theta}^s}=\frac{k_{p-pll}E_d^s s+E_d^s k_{i-pll}}{s^2+k_{p-pll}E_d^s s+E_d^s k_{i-pll}} \tag{23}$$

The bandwidth of the PLL can be defined as the -3dB point frequency of Eq.(23), which is approximately equal to:

$$f_{bw-pll}\approx\frac{k_{p-pll}E_d^s}{2\pi} \tag{24}$$

By now, all of the unknown transfer function matrices have already been solved. The next step is to calculate the impedance of the PCS by reduction of the block diagram in Fig. 3. After eliminating the feedback loops, the expression of Z_{out} is obtained as:

$$\begin{aligned}Z_{out}=&-[C_2\left(I+F_1G_{PI-C}C_1-F_1G_{DE}C_1\right)^{-1}\\&\times\left(F_1G_{PLL}^{e-u}-F_1G_{PI-C}G_{PLL}^{e-i}+F_2+F_1G_{DE}G_{PLL}^{e-i}\right)]^{-1}\end{aligned} \tag{25}$$

(d) Stability analysis.

An analysis is carried out with a Nyquist diagram of the impedance ratio Z_g/Z_{out}. The parameters are listed in Table I. They are identical to the three-phase downscaled prototype introduced in section IV.

Fig. 5(a) shows a Nyquist plot when the PCS is discharging. Fig. 5(b) shows a similar plot when the PCS is charging. Both Nyquist plots include two loci indicating the eigenvalue position of the impedance ratio in the complex plane. After that, the GNC is applied to predict the stability condition of the PCS under a weak grid. In the experimental environment, the grid inductance L_g is set to be much larger than its resistance.

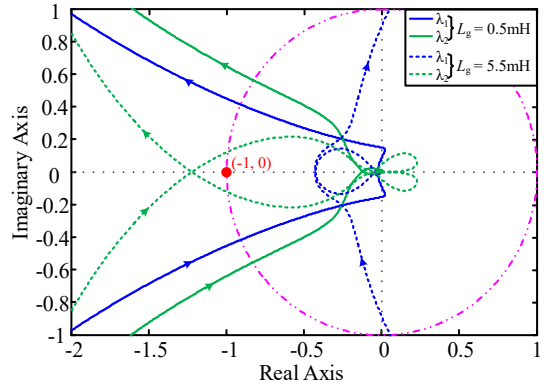

(a)

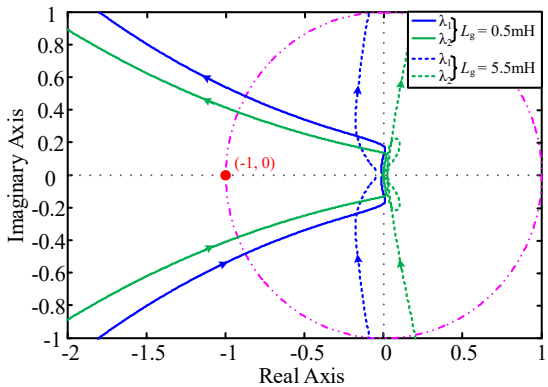

(b)

Fig. 5. Nyquist diagram of the impedance ratio.

Therefore, R_g has little effect on the loci and is omitted in the analysis[28].

As shown in Fig. 5(a), when connecting to a stiff grid (L_g is set to 0.5mH), neither of the characteristic loci encircle the critical point (-1,0). Hence, system stability is guaranteed. However, when connecting to a weak grid (L_g is set to 5.5mH), the second characteristic loci encircles the critical point (-1,0). Thus, the system trends to be unstable. Fig. 5(a) indicates that the relative stability of the PCS deteriorates rapidly when L_g becomes larger, and even becomes unstable when L_g exceeds the threshold value. This instability is largely aroused by the interaction between Z_{out} and Z_g. It causes the PCS to exhibit an oscillation and resonance phenomenon that leads to a poor power quality at the PCC point.

In the same time, stability problem seems non-essential when battery is charging. As illustrated in Fig. 5(b), none of the characteristic loci encircle the critical point while the PCS absorbs active power from grid. Therefore, the system keeps inherently stable both in stiff and weak grids in the charging condition.

III. VIRTUAL RESISTOR BASED CONTROL METHOD

From the point of view of the circuit fundamentals, one acceptable and commonly used solution to suppress the

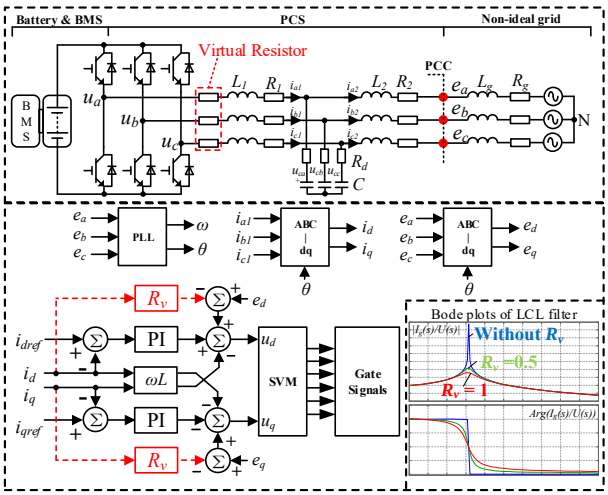

Fig. 6. Diagram of the proposed control method.

amplitude of the resonance is to place damping resistors in the system. This is also appropriate in tackling the instability problem described in the former section because the damping resistor can increase the output impedance of the PCS, which provides better rejection to the influence of Z_g. Since it can be illustrated that if Z_{out} is close to infinity, a native current source is always stable regardless of whether Z_g exists or not.

Nevertheless, the major drawback of a passive damping resistor is that it consumes a large amount of energy. This needless consumption significantly decreases the cycle efficiency and makes the thermal dissipation design more difficult, which should be carefully avoided in a PCS. Therefore, a control method adopting a virtual resistor is proposed in this paper for purpose of improving the performance of a PCS when connecting to a weak grid. A block diagram of the control method is shown in Fig. 6. The differences between the proposed and conventional methods are emphasized by red dashed lines. Two feedforward paths are added and no extra sample signal is necessary in this control method. If value of the resistance R_v is equal to zero, the proposed current control loop transforms backward into the conventional method discussed in section II.

The relations in Eq. (25) provide an insight into the impact from virtual resistors.

$$\begin{cases} L_1 \dfrac{di_{d1}}{dt} + R_1 i_{d1} = u_d - R_v i_{d1} - u_{cd} \\ L_1 \dfrac{di_{q1}}{dt} + R_1 i_{q1} = u_q - R_v i_{q1} - u_{cd} \end{cases} \tag{25}$$

Move the terms including R_v to the left side. Then Eq. (25) can be rewritten as:

$$\begin{cases} L_1 \dfrac{di_{d1}}{dt} + (R_v + R_1) i_{d1} = u_d - u_{cd} \\ L_1 \dfrac{di_{q1}}{dt} + (R_v + R_1) i_{q1} = u_q - u_{cq} \end{cases} \tag{26}$$

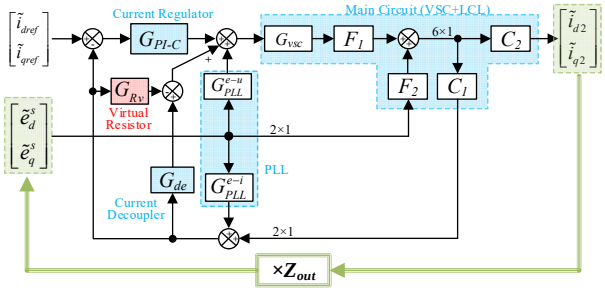

Fig. 7. Small-signal model of a PCS with virtual resistors.

Adding the feedforward paths as illustrated in Fig. 6 is equivalent to inserting a resistor in series with L_1 to damp the resonance. The frequency characteristics of the LCL filter is also given in the right bottom of Fig. 6, which shows that the resonant peak is effectively repressed by R_v. It is important to remark that R_v is not a real resistor. Thus, no extra power loss occurs on R_v. Moreover, it is also advantageous that virtual resistor can be adjusted to any desired value to achieve a trade-off between stability and speed. By adding virtual resistors into the circuit, the block diagram of a PCS in Fig. 3 transforms to Fig. 7.

The matrix G_{RV} to represent the virtual resistor is defined as:

$$G_{Rv} = \begin{pmatrix} R_v & 0 \\ 0 & R_v \end{pmatrix} \tag{27}$$

The expression of the impedance Z_{out} becomes:

$$\begin{aligned} Z_{out} = -[C_2 \left(I + F_1 G_0 C_1\right)^{-1} \cdot \\ \left(F_1 G_{PLL}^{e-u} - F_1 G_0 G_{PLL}^{e-i} + F_2\right)]^{-1} \end{aligned} \tag{28}$$

Where G_0 is equal to:

$$G_0 = G_{PI-C} - G_{DE} - G_{Rv} \tag{29}$$

A stability analysis is also carried out by a Nyquist diagram and GNC. Fig.8 shows a Nyquist plot of the impedance ratio Z_g/Z_{out} when the PCS is discharging with or without virtual resistors. L_g is equal to 5.5mH in Fig. 8(a), which corresponds with Fig. 5(a). The results when L_g is equal to 10.0 mH are also given in Fig. 8(b). It can be observed in Fig. 8 that the adoption of R_v can push the characteristic locus of λ_2 away from the critical point. Thus the whole system trends to be more stable.

The Nyquist locus exactly crossing the critical point is an important reference for selecting an appropriate value for the virtual resistor. This condition can be defined as marginally stable (M.S.) as depicted in Fig. 8. R_v corresponding to a M.S. locus determines the minimum value of the virtual resistor, which is denoted as $R_{v\text{-}min}$. For example, $R_{v\text{-}min}$ is equal to 0.42Ω in Fig. 8(a) and to 0.75Ω in Fig. 8(b). It can be seen that if R_v is less than $R_{v\text{-}min}$, the locus encircles the critical point, leading to an unstable system. Moreover, as shown in Fig. 5(a), if L_g is equal to 0.5mH, the cascaded system is naturally stable even without a virtual resistor. In such a case, $R_{v\text{-}min}$ is equal to zero.

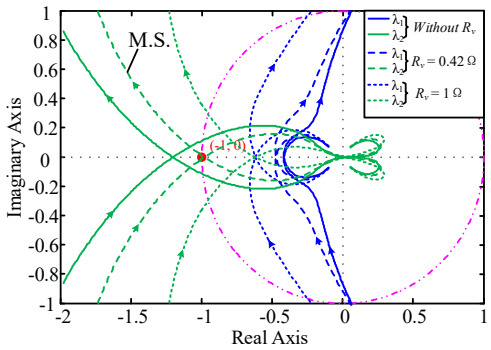

(a)

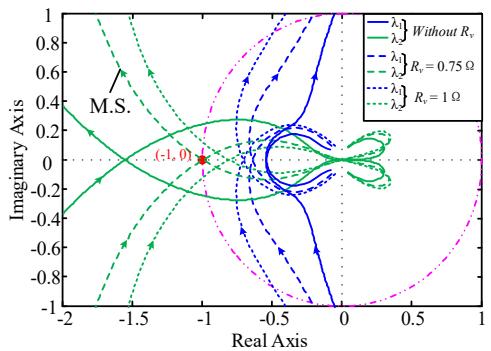

(b)

Fig. 8. Nyquist diagram of the impedance ratio with different R_v.

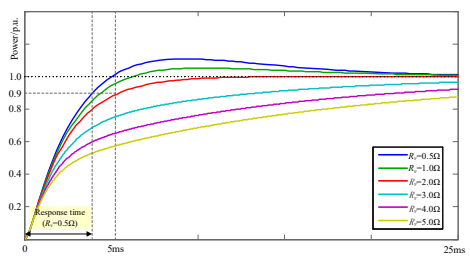

(a)

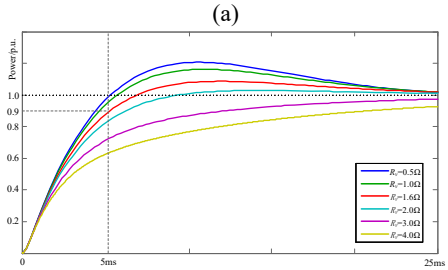

(b)

Fig. 9. Step response of a PCS with different R_v.

Response time t_r is another important technical specification in a PCS. It is defined as the rise time from the receipt of the instruction until the output power reaches 90% of the rating value. t_r represents the rapidity of the PCS. In this paper, t_r should be shorter than 5ms, one quarter of the line cycle. To make it more comprehensive, Fig. 9 compares the step response of the PCS with different values of R_v. According to Fig. 9, it can be deduced that although increasing R_v makes the system more stable, the transient characteristics obviously deteriorates. Thus, its value should not be chosen too large to satisfy the dynamic requirements. The maximum value of the virtual resistor constrained by t_r is denoted as $R_{v\text{-}max}$. Similarly, a unique $R_{v\text{-}max}$ exists with correspondence to a certain value of L_g. Take Fig. 9(a) for instance, $R_{v\text{-}max}$ is approximately equal to 2.0 ohms in this condition, since the PCS can no longer track the power reference fast enough if R_v is chosen to be more than 2.0 ohms.

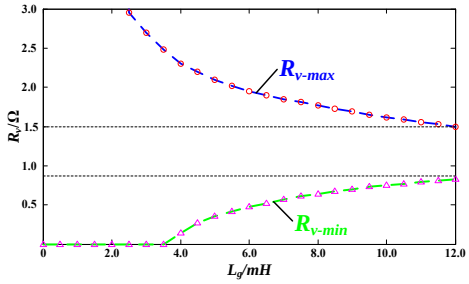

Fig. 10. The selection criteria of the virtual resistor value.

Other values of $R_{v\text{-}min}$ and $R_{v\text{-}max}$ relative to different grid impedances can be obtained in the same manner. In conclusion, a reasonable value for the virtual resistor is located in the range between $R_{v\text{-}min}$ and $R_{v\text{-}max}$ as shown in Fig. 10.

IV. Experimental Verification

A downscaled PCS prototype with a DSP controller (Texas Instruments, TMS320F28335) and an FPGA cooperator (Xilinx, XC3S200AN) is developed and tested in laboratory in order to verify the theoretical analysis and control method proposed in this paper. The parameters of the prototype are given in Table I. Fig. 11 is a photo of the experimental platform. Fig. 12 illustrates the experimental set-up of the impedance measurement.

In the first place, the impedance Z_{out} of the PCS is measured by voltage perturbation injection as shown in Fig. 13. Fig. 14(a) gives test results of Z_{out} when the PCS is charging, while Fig. 14(b) gives measured results when the PCS is discharging. The measured value of Z_{out} is in good agreement with its theoretical expression.

Fig. 15(a)-(c) show measured waveforms of the grid voltage and current when the PCS discharges at the rated power with different L_g. The PCS uses a traditional control method in this case. The total harmonic distortion (THD) of the grid current is calculated off-line in MATLAB. The THD of the grid current shown in Fig. 15(b) is equal to 12.3%, which is much higher than the THD of the current given in Fig.15(a).

By comparing Fig. 15(a)-(c), it can be deduced that the stability of the PCS deteriorates when L_g becomes larger. Note that in Fig. 15(c), the manual cut-in of L_g is executed because the PCS cannot operate normally when L_g=5.5mH. After inserting L_g into the circuit, the grid current runs out of control immediately until tripping an overcurrent fault to shut down the PCS.

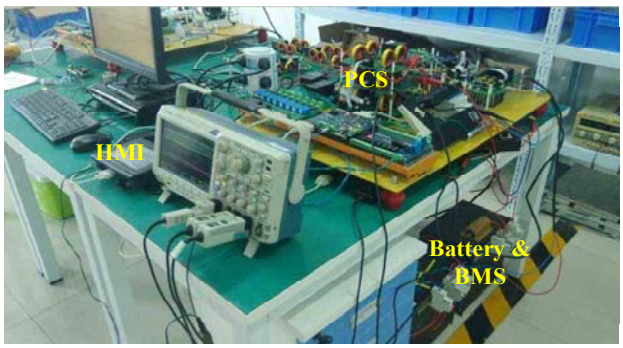

Fig. 11. Photo of the down-scaled prototype.

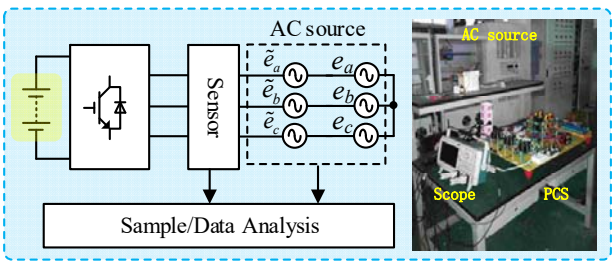

Fig. 12. Experimental set-up for impedance measurement.

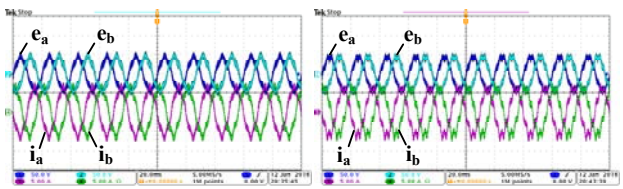

Fig. 13. Voltage perturbation injection and its response.

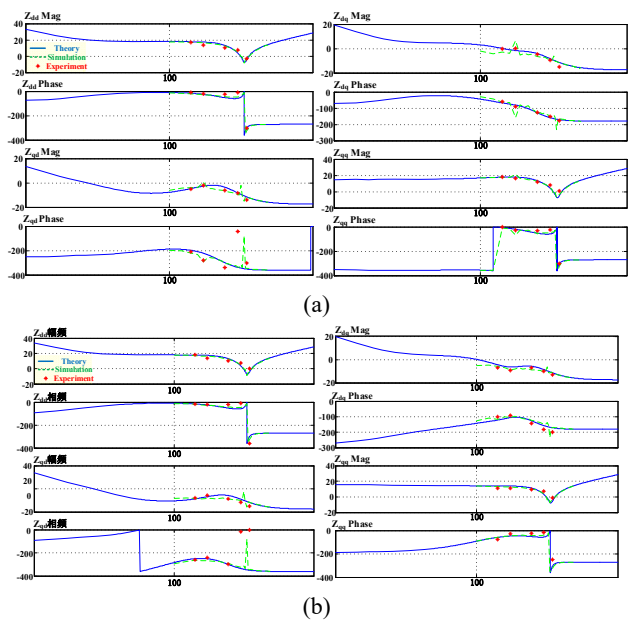

(a)

(b)

Fig. 14. Experimental results of the impedance measurement.

Fig. 15(d) shows the measured waveforms under the charging condition. On the other hand, although the same conventional control method is used, the PCS charging at the rated power is still stable even when L_g is equal to 5.5mH.

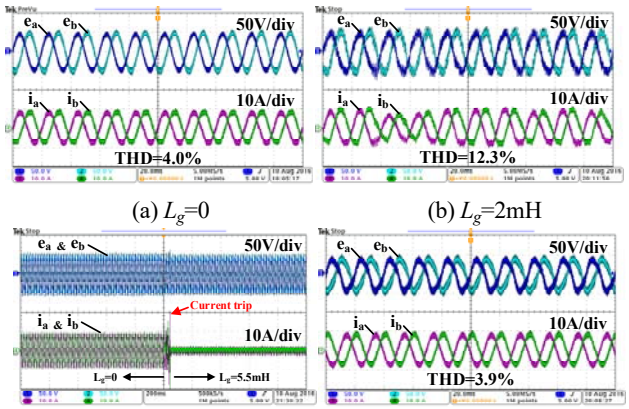

(a) L_g=0 (b) L_g=2mH

(c) L_g=5.5mH (d) L_g=5.5mH

Fig. 15. Tested waveforms under different grid conditions.

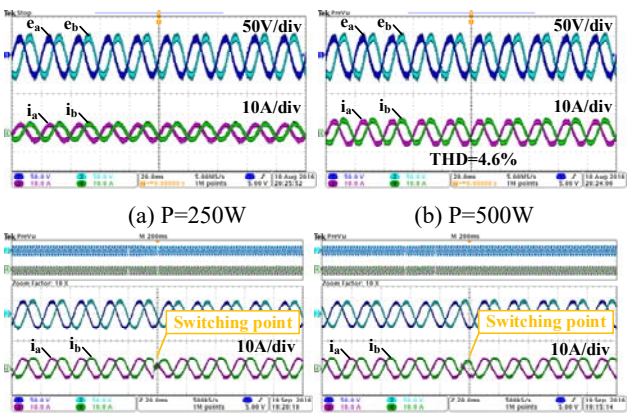

(a) P=250W (b) P=500W

(c) (d)

Fig. 16. Tested waveforms of the PCS with virtual resistors.

These experimental results validate the result of the stability analysis based on an impedance model in section II.

Fig 16. shows measured waveforms of the prototype with L_g=5.5mH after the adoption of virtual resistors. The value of R_v is equal to 1.0 ohm. The discharging power is 250W in Fig. 16(a) and 500W in Fig. 16(b). It can be seen that the proposed control method provides an obvious improvement in power quality and stability under a weak grid. Compared to Fig. 15(b), the harmonic analysis results indicate that the THD of the grid current decreases to 4.6%. The transient response is also tested and shown in Fig. 16(c)-(d). The PCS switches from discharging to charging in Fig.16(c) and from charging to discharging in Fig. 16(d). The duration of the transient is no longer than half a cycle, which is generally acceptable in BESS applications.

For comparison, Fig. 17(a) shows measured waveforms of the PCS under a weak grid based on the control method investigated in [26]. The output power is equal to 500W. Although the control strategy presented in [26] obtains results that are similar to those of this paper, it increases the overall cost because of the extra capacitor current transducers. Fig. 17(b) shows measured waveforms of the PCS in the same condition based on the virtual inductor concept presented in

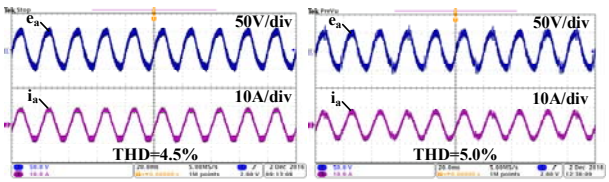

(a) (b)

Fig. 17. Tested waveforms of the PCS using the improving control method presented in [26][29].

[29]. However, the increase of the virtual inductor is not effective enough to stabilize the PCS because the adoption of the differential element is susceptible to interference, which leads to some glitches in the output current.

V. CONCLUSION

In this paper, the impedance model of a PCS with an LCL-filter applied in a BESS is carefully studied. Moreover, a novel control method based on virtual resistors is proposed. The analysis based on the impedance model and the general Nyquist criterion shows that the PCS tends to be unstable under a weak grid, and that the adoption of virtual resistors can stabilize the overall system to an acceptable condition. The selection criteria of R_v has been analyzed from the point of a trade-off between stability and dynamic performance. A down-scaled prototype is finally established. The experimental results verify the feasibility of the proposed control method. Better performance is obtained under a weak grid after placing virtual resistors into the PCS.

APPENDIX

Matrix A in formula (12) is equal to:

$$\begin{bmatrix} (R_d-R_1)/L_1 & \omega & -R_d/L_1 & 0 & -1/L_1 & 0 \\ -\omega & (R_d-R_1)/L_1 & 0 & -R_d/L_1 & 0 & -1/L_1 \\ R_d/L_2 & 0 & -(R_d+R_2)/L_2 & \omega & 1/L_2 & 0 \\ 0 & R_d/L_2 & -\omega & -(R_d+R_2)/L_2 & 0 & 1/L_2 \\ 1/C & 0 & -1/C & 0 & 0 & \omega \\ 0 & 1/C & 0 & -1/C & -\omega & 0 \end{bmatrix}$$

Matrix B in formula (12) is equal to:

$$\begin{bmatrix} 1/L_1 & 0 & 0 & 0 \\ 0 & 1/L_1 & 0 & 0 \\ 0 & 0 & -1/L_2 & 0 \\ 0 & 0 & 0 & -1/L_2 \\ 0 & 0 & 0 & 0 \\ 0 & 0 & 0 & 0 \end{bmatrix}$$

ACKNOWLEDGMENT

The work in this paper was supported by National Natural Science Foundation of China (No. 51641703).

REFERENCES

[1] J. M. Carrasco, L. G. Franquelo, J. T. Bialasiewicz, E. Galvan, R. C. PortilloGuisado, M. A. M. Prats, J. I. Leon, and N. Moreno-Alfonso, "Power-electronic systems for the grid integration of renewable energy sources: a survey," *IEEE Trans. Ind. Electron.*, Vol. 53, No. 4, pp. 1002-1016, Jun. 2006.

[2] O. Abdel-Rahim and H. Funato, "An experimental investigation of modified predictive hysteresis control based MPPT strategy for PV applications," in *IEEE Energy Conversion Congress and Exposition (ECCE)*, pp. 6450-6454, Sep. 2015.

[3] J. P. Barton and D. G. Infield, "Energy storage and its use with intermittent renewable energy," *IEEE Trans. Energy Convers.*, Vol. 19, No. 2, pp. 441-448, Jun. 2004.

[4] S. Vazquez, S. M. Lukic, E. Galvan, L. G. Franquelo, and J. M. Carrasco, "Energy storage systems for transport and grid applications," *IEEE Trans. Ind. Electron.*, Vol. 57, No. 12, pp. 3881-3895, Dec. 2011.

[5] D. M. Rastler, "Electricity energy storage technology options: a white paper primer on applications, costs and benefits," *Electric Power Research Institute*, 2010.

[6] K. C. Divya and J. Østergaard, "Battery energy storage technology for power systems—An overview," *Electric Power Systems Research*, Vol. 79, No. 4, pp. 511-520, Apr. 2009.

[7] X. Li, D. Hui, and X. Lai, "Battery energy storage station (BESS)-based smoothing control of photovoltaic (PV) and wind power generation fluctuations," *IEEE Trans. Sustain. Energy*, Vol. 4, No. 2, pp. 464-473, Apr. 2013.

[8] I. Serban and C. Marinescu, "Control strategy of three-phase battery energy storage systems for frequency support in microgrids and with uninterrupted supply of local loads," *IEEE Trans. Power Electron.*, Vol. 29, No. 9, pp. 5010-5020, Sep. 2014.

[9] L. Maharjan, S. Inoue, and H. Akagi, "A transformerless energy storage system based on a cascade multilevel pwm converter with star configuration," *IEEE Trans. Ind. Appl.*, Vol. 44, No. 5, pp. 1621-1630, Sep./Oct. 2008.

[10] N. M. L. Tan, T. Abe, and H. Akagi, "Design and performance of a bidirectional isolated DC–DC converter for a battery energy storage system," *IEEE Trans. Power Electron.*, Vol. 27, No. 3, pp. 1237-1248, Mar. 2012.

[11] K.-Y. Lo, Y.-M. Chen, and Y.-R. Chang, "Bi-directional single-stage grid-connected inverter for battery energy storage system," *IEEE Trans. Ind. Electron.*, Vol. PP, No. 99, pp. 1-1, Apr. 2016.

[12] H. Akagi, Y. Kanazawa, and A. Nabae, "Instantaneous reactive power compensators comprising switching devices without energy storage components," *IEEE Trans. Ind. Appl.*, Vol. IA-20, No. 3, pp. 625-630, May 1984.

[13] D. Ikni, M. B. Camara, and B. Dakyo, "Offshore wind farms energy injection in the electrical grid - Lithium battery to mitigate power fluctuations," *International Journal of Renewable Energy Research*, Vol. 5, No. 4, pp. 1049-1061, Nov. 2015.

[14] M. Liserre, R. Teodorescu, and F. Blaabjerg, "Stability of photovoltaic and wind turbine grid-connected inverters for a large set of grid impedance values," *IEEE Trans. Power Electron.*, Vol. 21, No. 1, pp. 263-272, Jan. 2006.

[15] X. Wang, F. Blaabjerg, M. Liserre, Z. Chen, J. He, and Y. Li, "An active damper for stabilizing power-electronics-based AC systems," *IEEE Trans. Power Electron.*, Vol. 29, No. 7, pp. 3318-3329, Jul. 2014.

[16] J. Z. Zhou, H. Ding, S. Fan, Y. Zhang, and A. M. Gole, "Impact of short-circuit ratio and phase-locked-loop parameters on the small-signal behavior of a VSC-HVDC converter," *IEEE Trans. Power Del.*, Vol. 29, No. 5, pp. 2287-2296, Oct. 2014.
[17] B. Zeng, S. Ouyang, J. Zhang, H. Shi, G. Wu, and M. Zeng, "An analysis of previous blackouts in the world: Lessons for China's power industry," *Renewable and Sustainable Energy Reviews*, Vol. 42, pp. 1151-1163, Feb. 2015.
[18] J. Sun, "Impedance-based stability criterion for grid-connected inverters," *IEEE Trans. Power Electron.*, Vol. 26, No. 11, pp. 3075-3078, Nov. 2011.
[19] M. Cespedes and J. Sun, "Impedance modeling and analysis of grid-connected voltage-source converters," *IEEE Trans. Power Electron.*, Vol. 29, No. 3, pp. 1254-1261, Mar. 2014.
[20] B. Wen, D. Boroyevich, R. Burgos, P. Mattavelli, and Z. Shen, "Analysis of D-Q small-signal impedance of grid-tied inverters," *IEEE Trans. Power Electron.*, Vol. 31, No. 1, pp. 675-687, Jan. 2016.
[21] B. Wen, D. Boroyevich, P. Mattavelli, Z. Shen, and R. Burgos, "Influence of phase-locked loop on input admittance of three-phase voltage-source converters," in *Twenty-Eighth Annual IEEE Applied Power Electronics Conference and Exposition (APEC)*, pp. 897-904, Mar. 2013.
[22] L. Fan, Z. Miao, "Nyquist-stability-criterion-based SSR explanation for type-3 wind generators," *IEEE Trans. Energy Convers.*, Vol. 27, No. 3, pp. 807-809, Sep. 2012.
[23] H. Liu and J. Sun, "Voltage stability and control of offshore wind farms with AC collection and HVDC transmission," *IEEE J. Emerg. Sel. Topics Power Electron.*, Vol. 2, No .4, pp. 1181-1189, Dec. 2014.
[24] J. Lyu, X. Cai, and M. Molinas, "Frequency domain stability analysis of MMC-based HVDC for wind farm integration," *IEEE J. Emerg. Sel. Topics Power Electron.*, Vol. 4, No. 1, pp. 141-151, Mar. 2016.
[25] Y. Liu, W. Wu, Y. He, Z. Lin, F. Blaabjerg, and H. S.-H. Chung, "An efficient and robust hybrid damper for, LCL - or, LLCL -based grid-tied inverter with strong grid-side harmonic voltage effect rejection," *IEEE Trans. Ind. Electron.*, Vol. 63, No. 2, pp. 926-936, Feb. 2016.
[26] J. Dannehl, F. W. Fuchs, S. Hansen, and P. B. Thogersen, "Investigation of active damping approaches for PI-based current control of grid-connected PWM converters with LCL filters," *IEEE Trans. Ind. Appl.*, Vol. 46, No. 4, pp. 1509-1517, Jul./Aug. 2010.
[27] Y. Tian, P. C. Loh, F. Deng, Z. Chen, X. Sun, and Y, Hu, "Impedance coordinative control for cascaded converter in bidirectional application," *IEEE Trans. Ind. Appl.*, Vol. 52, No. 5, pp. 4084-4095, Sep./Oct. 2016.
[28] S. Cobreces, E. Bueno, F. J. Rodriguez, F. Huerta, and P. Rodriguez, "Influence analysis of the effects of an inductive-resistive weak grid over L and LCL filter current hysteresis controllers," in *European Conference on Power Electronics and Applications*, pp. 1-10, Sep. 2007.
[29] G. Liu, Y. Yang, P. Wang, W. Wang, and D. Xu, "Stability control method based on virtual inductance of grid-connected PV inverter under weak grid," in *39th Annual Conference of the IEEE Industrial Electronics Society (IECON)*, pp. 1867-1872, Nov. 2013.

Ning Gao was born in Haining, Zhejiang, China, in 1987. He received his B.S. degree in Electronics and Information Engineering from Zhejiang University, Hangzhou, China, in 2009; and his M.S. degree from Shanghai Jiao Tong University, Shanghai, China, in 2011, where he is presently working towards his Ph.D. degree. His current research interests include power converters applied in battery energy storage systems, efficiency analysis and the optimization of power conversion systems.

Shun Sang was born in Jiangsu, China, in 1991. He received his B.S. degree in Electrical Engineering from the China University of Mining and Technology, Jiangsu, China, in 2014. He is presently working towards his Ph.D. degree in the Wind Power Research Center, Shanghai Jiao Tong University, Shanghai, China. His current research interests include the interaction stability issues of wind power converters in AC grids.

Rui Li was born in Qingdao, China, in 1980. He received his M.S. degree in Electrical Engineering from the Nanjing University of Aeronautics and Astronautics, Nanjing, China, in 2005; and his Ph.D. degree in Electrical Engineering from Zhejiang University, Hangzhou, China, in 2010. From September 2008 to August 2009, he was an Academic Guest with the Power Electronic Systems Laboratory, Swiss Federal Institute of Technology, Zurich, Switzerland. From July 2014 to August 2015, he was a Postdoctoral Research Scholar in the Center for Advanced Power Systems, Department of Electrical and Computer Engineering, College of Engineering, Florida State University, Tallahassee, FL, USA. Since December 2010, he has been with the Department of Electrical Engineering, School of Electronics, Information and Electrical Engineering, Shanghai Jiao Tong University, Shanghai, China, where he is presently working as an Associate Professor. He received an IEEE Power Electronics Society Transactions Second Prize Paper Award in 2015. His current research interests include the application of power electronics in renewable energy conversion.

Xu Cai received his B.S. degree in Electrical Engineering from Southeast University, Nanjing, China, in 1983; and his M.S. and Ph.D. degrees from the China University of Mining and Technology, in 1988 and 2000, respectively. He was with the Department of Electrical Engineering, China University of Mining and Technology, as an Associate Professor from 1989 to 2001. He joined Shanghai Jiao Tong University, Shanghai, China, as a Professor in 2002, and has been the Director of the Wind Power Research Center of Shanghai Jiao Tong University since 2008. His current research include power electronics, and renewable energy exploitation and utilization.